

# Dual-modality fiber-based OCT-TPL imaging system for simultaneous microstructural and molecular analysis of atherosclerotic plaques

Tianyi Wang,<sup>1,\*</sup> Austin McElroy,<sup>1</sup> David Halaney,<sup>2,3</sup> Deborah Vela,<sup>4</sup>  
Edmund Fung,<sup>1</sup> Shafat Hossain,<sup>1</sup> Jennifer Phipps,<sup>2</sup> Bingqing Wang,<sup>1</sup> Biwei Yin,<sup>1</sup>  
Marc D. Feldman,<sup>2,3</sup> and Thomas E. Milner<sup>1</sup>

<sup>1</sup>Department of Biomedical Engineering, University of Texas at Austin, 1 University Station C0800, Austin, Texas 78712, USA

<sup>2</sup>Division of Cardiology, University of Texas Health Science Center, 7703 Floyd Curl Drive, San Antonio, Texas 78229, USA

<sup>3</sup>South Texas Veterans Health Care System, San Antonio, Texas 78229, USA

<sup>4</sup>Texas Heart Institute, Houston, Texas 77030, USA

\*Tianyi.Wang@utexas.edu

**Abstract:** New optical imaging techniques that provide contrast to study both the anatomy and composition of atherosclerotic plaques can be utilized to better understand the formation, progression and clinical complications of human coronary artery disease. We present a dual-modality fiber-based optical imaging system for simultaneous microstructural and molecular analysis of atherosclerotic plaques that combines optical coherence tomography (OCT) and two-photon luminescence (TPL) imaging. Experimental results from *ex vivo* human coronary arteries show that OCT and TPL optical contrast in recorded OCT-TPL images is complimentary and in agreement with histological analysis. Molecular composition (e.g., lipid and oxidized-LDL) detected by TPL imaging can be overlaid onto plaque microstructure depicted by OCT, providing new opportunities for atherosclerotic plaque identification and characterization.

©2015 Optical Society of America

**OCIS codes:** (110.4500) Optical coherence tomography; (190.1900) Diagnostic applications of nonlinear optics; (190.4370) Nonlinear optics, fibers; (170.6280) Spectroscopy, fluorescence and luminescence; (170.6935) Tissue characterization.

## References and links

1. A. S. Go, D. Mozaffarian, V. L. Roger, E. J. Benjamin, J. D. Berry, M. J. Blaha, S. Dai, E. S. Ford, C. S. Fox, S. Franco, H. J. Fullerton, C. Gillespie, S. M. Hailpern, J. A. Heit, V. J. Howard, M. D. Huffman, S. E. Judd, B. M. Kissela, S. J. Kittner, D. T. Lackland, J. H. Lichtman, L. D. Lisabeth, R. H. Mackey, D. J. Magid, G. M. Marcus, A. Marelli, D. B. Matchar, D. K. McGuire, E. R. Mohler 3rd, C. S. Moy, M. E. Mussolino, R. W. Neumar, G. Nichol, D. K. Pandey, N. P. Paynter, M. J. Reeves, P. D. Sorlie, J. Stein, A. Towfighi, T. N. Turan, S. S. Virani, N. D. Wong, D. Woo, and M. B. Turner; American Heart Association Statistics Committee and Stroke Statistics Subcommittee, "Heart disease and stroke statistics--2014 update: a report from the American Heart Association," *Circulation* **129**(3), e28–e292 (2014).
2. P. Libby, P. M. Ridker, and A. Maseri, "Inflammation and atherosclerosis," *Circulation* **105**(9), 1135–1143 (2002).
3. P. Libby and P. Theroux, "Pathophysiology of coronary artery disease," *Circulation* **111**(25), 3481–3488 (2005).
4. A. R. Lucas, R. Korol, and C. J. Pepine, "Inflammation in atherosclerosis: some thoughts about acute coronary syndromes," *Circulation* **113**(17), e728–e732 (2006).
5. K. Skålén, M. Gustafsson, E. K. Rydberg, L. M. Hultén, O. Wiklund, T. L. Innerarity, and J. Borén, "Subendothelial retention of atherogenic lipoproteins in early atherosclerosis," *Nature* **417**(6890), 750–754 (2002).
6. N. Leitinger, "Oxidized phospholipids as modulators of inflammation in atherosclerosis," *Curr. Opin. Lipidol.* **14**(5), 421–430 (2003).
7. J. D. Smith, E. Trogan, M. Ginsberg, C. Grigaux, J. Tian, and M. Miyata, "Decreased atherosclerosis in mice deficient in both macrophage colony-stimulating factor (op) and apolipoprotein E," *Proc. Natl. Acad. Sci. U.S.A.* **92**(18), 8264–8268 (1995).

8. L. Boring, J. Gosling, M. Cleary, and I. F. Charo, "Decreased lesion formation in CCR2<sup>-/-</sup> mice reveals a role for chemokines in the initiation of atherosclerosis," *Nature* **394**(6696), 894–897 (1998).
9. L. Gu, Y. Okada, S. K. Clinton, C. Gerard, G. K. Sukhova, P. Libby, and B. J. Rollins, "Absence of monocyte chemoattractant protein-1 reduces atherosclerosis in low density lipoprotein receptor-deficient mice," *Mol. Cell* **2**(2), 275–281 (1998).
10. Y. Fukumoto, P. Libby, E. Rabkin, C. C. Hill, M. Enomoto, Y. Hirouchi, M. Shiomi, and M. Aikawa, "Statins alter smooth muscle cell accumulation and collagen content in established atheroma of watanabe heritable hyperlipidemic rabbits," *Circulation* **103**(7), 993–999 (2001).
11. M. J. Davies, P. D. Richardson, N. Woolf, D. R. Katz, and J. Mann, "Risk of thrombosis in human atherosclerotic plaques: role of extracellular lipid, macrophage, and smooth muscle cell content," *Br. Heart J.* **69**(5), 377–381 (1993).
12. A. C. van der Wal, A. E. Becker, C. M. van der Loos, and P. K. Das, "Site of intimal rupture or erosion of thrombosed coronary atherosclerotic plaques is characterized by an inflammatory process irrespective of the dominant plaque morphology," *Circulation* **89**(1), 36–44 (1994).
13. W. Insull, Jr. and G. E. Bartsch, Jr., "Cholesterol, triglyceride, and phospholipid content of intima, media, and atherosclerotic fatty streak in human thoracic aorta," *J. Clin. Invest.* **45**(4), 513–523 (1966).
14. J. R. Guyton and K. F. Klemp, "Development of the atherosclerotic core region. Chemical and ultrastructural analysis of microdissected atherosclerotic lesions from human aorta," *Arterioscler. Thromb.* **14**(8), 1305–1314 (1994).
15. J. Sanz and Z. A. Fayad, "Imaging of atherosclerotic cardiovascular disease," *Nature* **451**(7181), 953–957 (2008).
16. A. H. Gershlick, M. de Belder, J. Chambers, D. Hackett, R. Keal, A. Kelion, S. Neubauer, D. J. Pennell, M. Rothman, M. Signy, and P. Wilde, "Role of non-invasive imaging in the management of coronary artery disease: An assessment of likely change over the next 10 years. A report from the British Cardiovascular Society Working Group," *Heart* **93**(4), 423–431 (2007).
17. R. A. Trivedi, C. Mallawarachi, J. M. U-King-Im, M. J. Graves, J. Horsley, M. J. Goddard, A. Brown, L. Wang, P. J. Kirkpatrick, J. Brown, and J. H. Gillard, "Identifying inflamed carotid plaques using in vivo USPIO-enhanced MR imaging to label plaque macrophages," *Arterioscler. Thromb. Vasc. Biol.* **26**(7), 1601–1606 (2006).
18. F. Hyafil, J. C. Cornily, J. E. Feig, R. Gordon, E. Vucic, V. Amirbekian, E. A. Fisher, V. Fuster, L. J. Feldman, and Z. A. Fayad, "Noninvasive detection of macrophages using a nanoparticulate contrast agent for computed tomography," *Nat. Med.* **13**(5), 636–641 (2007).
19. A. Tawakol, R. Q. Migrino, G. G. Bashian, S. Bedri, D. Vermylen, R. C. Cury, D. Yates, G. M. LaMuraglia, K. Furie, S. Houser, H. Gewirtz, J. E. Muller, T. J. Brady, and A. J. Fischman, "In vivo 18F-fluorodeoxyglucose positron emission tomography imaging provides a noninvasive measure of carotid plaque inflammation in patients," *J. Am. Coll. Cardiol.* **48**(9), 1818–1824 (2006).
20. F. A. Jaffer, D. E. Kim, L. Quinti, C. H. Tung, E. Aikawa, A. N. Pande, R. H. Kohler, G. P. Shi, P. Libby, and R. Weissleder, "Optical visualization of cathepsin K activity in atherosclerosis with a novel, protease-activatable fluorescence sensor," *Circulation* **115**(17), 2292–2298 (2007).
21. S. Sethuraman, S. R. Aglyamov, J. H. Amirian, R. W. Smalling, and S. Y. Emelianov, "Intravascular photoacoustic imaging using an IVUS imaging catheter," *IEEE Trans. Ultrason. Ferroelectr. Freq. Control* **54**(5), 978–986 (2007).
22. G. J. Tearney, H. Yabushita, S. L. Houser, H. T. Aretz, I. K. Jang, K. H. Schlendorf, C. R. Kauffman, M. Shishkov, E. F. Halpern, and B. E. Bouma, "Quantification of macrophage content in atherosclerotic plaques by optical coherence tomography," *Circulation* **107**(1), 113–119 (2003).
23. M. F. Kircher, J. Grimm, F. K. Swirski, P. Libby, R. E. Gerszten, J. R. Allport, and R. Weissleder, "Noninvasive in vivo imaging of monocyte trafficking to atherosclerotic lesions," *Circulation* **117**(3), 388–395 (2008).
24. B. Wang, J. L. Su, J. Amirian, S. H. Litovsky, R. Smalling, and S. Emelianov, "Detection of lipid in atherosclerotic vessels using ultrasound-guided spectroscopic intravascular photoacoustic imaging," *Opt. Express* **18**(5), 4889–4897 (2010).
25. J. Bec, D. M. Ma, D. R. Yankelevich, J. Liu, W. T. Ferrier, J. Southard, and L. Marcu, "Multispectral fluorescence lifetime imaging system for intravascular diagnostics with ultrasound guidance: in vivo validation in swine arteries," *J. Biophotonics* **7**(5), 281–285 (2014).
26. X. Li, J. Li, J. Jing, T. Ma, S. Liang, J. Zhang, D. Mohar, A. Raney, S. Mahon, M. Brenner, P. Patel, K. K. Shung, Q. Zhou, and Z. Chen, "Integrated IVUS-OCT Imaging for Atherosclerotic Plaque Characterization," *IEEE J. Sel. Top. Quantum Electron.* **20**(2), 7100108 (2014).
27. H. Yoo, J. W. Kim, M. Shishkov, E. Namati, T. Morse, R. Shubochkin, J. R. McCarthy, V. Ntziachristos, B. E. Bouma, F. A. Jaffer, and G. J. Tearney, "Intra-arterial catheter for simultaneous microstructural and molecular imaging in vivo," *Nat. Med.* **17**(12), 1680–1684 (2011).
28. T. T. Le, I. M. Langohr, M. J. Locker, M. Sturek, and J. X. Cheng, "Label-free molecular imaging of atherosclerotic lesions using multimodal nonlinear optical microscopy," *J. Biomed. Opt.* **12**(5), 054007 (2007).
29. M. van Zandvoort, W. Engels, K. Douma, L. Beckers, M. Oude Egbrink, M. Daemen, and D. W. Slaaf, "Two-photon microscopy for imaging of the (atherosclerotic) vascular wall: A proof of concept study," *J. Vasc. Res.* **41**(1), 54–63 (2004).
30. A. Zoumi, X. A. Lu, G. S. Kassab, and B. J. Tromberg, "Imaging coronary artery microstructure using second-

- harmonic and two-photon fluorescence microscopy,” *Biophys. J.* **87**(4), 2778–2786 (2004).
31. T. Boulesteix, A. M. Pena, N. Pagès, G. Godeau, M. P. Sauviat, E. Beaufrepaire, and M. C. Schanne-Klein, “Micrometer scale ex vivo multiphoton imaging of unstained arterial wall structure,” *Cytometry A* **69A**(1), 20–26 (2006).
  32. E. Beaufrepaire, L. Moreaux, F. Amblard, and J. Mertz, “Combined scanning optical coherence and two-photon-excited fluorescence microscopy,” *Opt. Lett.* **24**(14), 969–971 (1999).
  33. S. Tang, T. B. Krasieva, Z. Chen, and B. J. Tromberg, “Combined multiphoton microscopy and optical coherence tomography using a 12-fs broadband source,” *J. Biomed. Opt.* **11**(2), 020502 (2006).
  34. C. Vinegoni, T. Ralston, W. Tan, W. Luo, D. L. Marks, and S. A. Boppart, “Integrated structural and functional optical imaging combining spectral-domain optical coherence and multiphoton microscopy,” *Appl. Phys. Lett.* **88**(5), 053901 (2006).
  35. B. Jeong, B. Lee, M. S. Jang, H. Nam, S. J. Yoon, T. Wang, J. Doh, B. G. Yang, M. H. Jang, and K. H. Kim, “Combined two-photon microscopy and optical coherence tomography using individually optimized sources,” *Opt. Express* **19**(14), 13089–13096 (2011).
  36. T. Wang, Q. Li, P. Xiao, J. Ahn, Y. E. Kim, Y. Park, M. Kim, M. Song, E. Chung, W. K. Chung, G. O. Ahn, S. Kim, P. Kim, S. J. Myung, and K. H. Kim, “Gradient index lens based combined two-photon microscopy and optical coherence tomography,” *Opt. Express* **22**(11), 12962–12970 (2014).
  37. J. Xi, Y. Chen, Y. Zhang, K. Murari, M. J. Li, and X. Li, “Integrated multimodal endomicroscopy platform for simultaneous en face optical coherence and two-photon fluorescence imaging,” *Opt. Lett.* **37**(3), 362–364 (2012).
  38. D. Kessler and R. V. Shack, “ȳ diagram, a powerful optical design method for laser systems,” *Appl. Opt.* **31**(15), 2692–2707 (1992).
  39. A. Beaudoin, “New technique for revealing latent fingerprints on wet, porous surfaces: Oil Red O,” *J. Forensic Ident.* **54**(4), 413–421 (2004).  
<http://www.vetmed.vt.edu/education/Curriculum/VM8054/Labs/Lab2/Examples/exvrmass.htm>
  40. O. E. Martinez, “3000 times grating compressor with positive group velocity dispersion: application to fiber compensation in 1.3–1.6 μm region,” *IEEE J. Quantum Electron.* **23**(1), 549–564 (1987).
  41. O. E. Martinez, “Design of high-power ultrashort pulse amplifiers by expansion and recompression,” *IEEE J. Quantum Electron.* **23**(8), 1385–1387 (1987).
  42. A. Mooradian, “Photoluminescence of metals,” *Phys. Rev. Lett.* **22**(5), 185–187 (1969).
  43. M. M. Arnida, M. M. Janát-Amsbury, A. Ray, C. M. Peterson, and H. Ghandehari, “Geometry and surface characteristics of gold nanoparticles influence their biodistribution and uptake by macrophages,” *Eur. J. Pharm. Biopharm.* **77**(3), 417–423 (2011).
  44. R. Shukla, V. Bansal, M. Chaudhary, A. Basu, R. R. Bhone, and M. Sastry, “Biocompatibility of gold nanoparticles and their endocytotic fate inside the cellular compartment: a microscopic overview,” *Langmuir* **21**(23), 10644–10654 (2005).
  45. X. Ji, R. Shao, A. M. Elliott, R. J. Stafford, E. Esparza-Coss, J. A. Bankson, G. Liang, Z.-P. Luo, K. Park, J. T. Markert, and C. Li, “Bifunctional Gold Nanoshells with a Superparamagnetic Iron Oxide-Silica Core Suitable for Both MR Imaging and Photothermal Therapy,” *J. Phys. Chem. C.* **111**(17), 6245–6251 (2007).
  46. S. Lal, S. E. Clare, and N. J. Halas, “Nanoshell-enabled photothermal cancer therapy: impending clinical impact,” *Acc. Chem. Res.* **41**(12), 1842–1851 (2008).
  47. T. Niidome, M. Yamagata, Y. Okamoto, Y. Akiyama, H. Takahashi, T. Kawano, Y. Katayama, and Y. Niidome, “PEG-modified gold nanorods with a stealth character for in vivo applications,” *J. Control. Release* **114**(3), 343–347 (2006).
  48. T. S. Hauck, A. A. Ghazani, and W. C. W. Chan, “Assessing the effect of surface chemistry on gold nanorod uptake, toxicity, and gene expression in mammalian cells,” *Small* **4**(1), 153–159 (2008).
  49. T. Wang, J. J. Mancuso, S. M. Kazmi, J. Dwelle, V. Sapozhnikova, B. Willsey, L. L. Ma, J. Qiu, X. Li, A. K. Dunn, K. P. Johnston, M. D. Feldman, and T. E. Milner, “Combined two-photon luminescence microscopy and OCT for macrophage detection in the hypercholesterolemic rabbit aorta using plasmonic gold nanorods,” *Lasers Surg. Med.* **44**(1), 49–59 (2012).
  50. L. L. Ma, M. D. Feldman, J. M. Tam, A. S. Paranjape, K. K. Cheruku, T. A. Larson, J. O. Tam, D. R. Ingram, V. Paramita, J. W. Villard, J. T. Jenkins, T. Wang, G. D. Clarke, R. Asmis, K. Sokolov, B. Chandrasekar, T. E. Milner, and K. P. Johnston, “Small multifunctional nanoclusters (nanoroses) for targeted cellular imaging and therapy,” *ACS Nano* **3**(9), 2686–2696 (2009).
  51. G. T. Boyd, Z. H. Yu, and Y. R. Shen, “Photoinduced luminescence from the noble metals and its enhancement on roughened surfaces,” *Phys. Rev. B Condens. Matter* **33**(12), 7923–7936 (1986).
  52. M. R. Beversluis, A. Bouhelier, and L. Novotny, “Continuum generation from single gold nanostructures through near-field mediated intraband transitions,” *Phys. Rev. B* **68**(11), 115433 (2003).
  53. T. Wang, D. Halaney, D. Ho, M. D. Feldman, and T. E. Milner, “Two-photon luminescence properties of gold nanorods,” *Biomed. Opt. Express* **4**(4), 584–595 (2013).
  54. M. B. Lilledahl, O. A. Haugen, C. de Lange Davies, and L. O. Svaasand, “Characterization of vulnerable plaques by multiphoton microscopy,” *J. Biomed. Opt.* **12**(4), 044005 (2007).
  55. W. Yu, J. C. Braz, A. M. Dutton, P. Prusakov, and M. Rekhter, “In vivo imaging of atherosclerotic plaques in apolipoprotein E deficient mice using nonlinear microscopy,” *J. Biomed. Opt.* **12**(5), 054008 (2007).
  56. A. C. Guyton and J. E. Hall, *Textbook of Medical Physiology*, 11th ed. (Philadelphia: Elsevier Saunders, 2005),

- pp. 849–851.
58. G. J. Tearney, M. E. Brezinski, S. A. Boppart, B. E. Bouma, N. Weissman, J. F. Southern, E. A. Swanson, and J. G. Fujimoto, "Catheter-based optical imaging of a human coronary artery," *Circulation* **94**(11), 3013 (1996).
  59. H. Yabushita, B. E. Bouma, S. L. Houser, H. T. Aretz, I. K. Jang, K. H. Schlendorf, C. R. Kauffman, M. Shishkov, D. H. Kang, E. F. Halpern, and G. J. Tearney, "Characterization of human atherosclerosis by optical coherence tomography," *Circulation* **106**(13), 1640–1645 (2002).
  60. J. E. Phipps, D. Vela, T. Hoyt, D. Halaney, J. J. Mancuso, L. M. Buja, R. Asmis, T. E. Milner, and M. D. Feldman, "Macrophages and intravascular optical coherence tomography bright spots: a quantitative study," *JACC Cardiovasc. Imaging* **8**(1), 63–72 (2015).
  61. T. Wang, J. J. Mancuso, V. Sapozhnikova, J. Dwelle, L. L. Ma, B. Willsey, S. M. Kazmi, J. Qiu, X. Li, R. Asmis, K. P. Johnston, M. D. Feldman, and T. E. Milner, "Dual-wavelength multifrequency photothermal wave imaging combined with optical coherence tomography for macrophage and lipid detection in atherosclerotic plaques using gold nanoparticles," *J. Biomed. Opt.* **17**(3), 036009 (2012).
  62. T. Q. Dinh, R. J. Tuch, and R. S. Schwartz, "Drug eluting stent," U.S. Patent: US5697967 A, issued date Dec 16, 1997.
  63. D. Lorensen, B. C. Quirk, M. Auger, W.-J. Madore, R. W. Kirk, N. Godbout, D. D. Sampson, C. Boudoux, and R. A. McLaughlin, "Dual-modality needle probe for combined fluorescence imaging and three-dimensional optical coherence tomography," *Opt. Lett.* **38**(3), 266–268 (2013).
  64. G. J. Tearney, S. Waxman, M. Shishkov, B. J. Vakoc, M. J. Suter, M. I. Freilich, A. E. Desjardins, W. Y. Oh, L. A. Bartlett, M. Rosenberg, and B. E. Bouma, "Three-dimensional coronary artery microscopy by intracoronary optical frequency domain imaging," *JACC Cardiovasc. Imaging* **1**(6), 752–761 (2008).
- 

## 1. Introduction

Cardiovascular disease takes a huge toll on our society and was responsible for at least 1 in every 3 deaths in the United States in 2010 [1]. Atherosclerosis is an inflammatory disease, progressing over time to the buildup of atherosclerotic plaques characterized by lipid deposition and inflammation in the arterial wall. Atherosclerotic plaque is prone to rupture and can induce clot formation, leading to stroke and acute myocardial infarction. Recent advances in basic and experimental science have established a fundamental role that underlying cellular and molecular mechanisms contribute to mechanical instability and increased risk of plaque rupture and subsequent clinical complications [2–4]. These mechanisms include infiltration and retention of low-density lipoprotein (LDL) [5,6], recruitment of macrophages [7–9], a decrease in smooth muscle cells and collagen synthesis [10,11], and thinning of the fibrous cap with an increased underlying lipid core size [12]. The major lipid species in atherosclerotic plaques is cholesterol which exists in both free and esterified forms [13]. The percentage of free cholesterol increases in lesion cores while cholesteryl ester enriches in lesion caps [14]. Thus, lipid deposition in relation to plaque microstructure (i.e., fibrous cap) represents an important early molecular marker that provides information relevant to the risk of future plaque rupture. *In vivo* lipid identification at a high resolution without using exogenous contrast agents is of great clinical value.

Currently, non-invasive imaging modalities including angiography, magnetic resonance imaging (MRI), computed tomography (CT), and positron emission tomography (PET) have been utilized to screen for atherosclerotic cardiovascular diseases in the human body (e.g., atherosclerotic plaques in the arterial wall) [15,16]. Catheter-based minimally-invasive imaging modalities including near-infrared fluorescence (NIRF), intravascular ultrasound (IVUS), intravascular photoacoustic imaging (IVPA) and intravascular optical coherence tomography (IVOCT) have been applied to image the structure or composition of specific blood vessels (e.g., coronary atherosclerosis) [17–22]. More recently, dual-modality imaging systems such as single-photon emission CT (SPECT)-CT, IVUS-IVPA, IVUS- fluorescence life-time imaging (FLIM), IVUS-IVOCT, and IVOCT-NIRF are being investigated to simultaneously detect plaque structure and composition with higher specificity [23–27]. Some disadvantages are that SPECT, IVPA, FLIM and NIRF do not provide a high resolution equivalent to OCT, and moreover, SPECT and NIRF require exogenous imaging contrast agents. Among the above single-/dual-modality imaging techniques, OCT provides the highest resolution and is the sole approach to visualize thin fibrous caps (<65  $\mu\text{m}$ ). However, use of OCT alone to identify atherosclerotic plaques is limited due to the poor scattering

contrast between lipid and other plaque components such as calcium and fibrous tissue. Two-photon luminescence (TPL) microscopy uses nonlinear absorption/emission properties of tissue and has been applied for *ex vivo/in vivo* plaque component characterization with cellular or subcellular resolution, including collagen, elastin fibers, calcium, oxidized-LDL and lipid deposits [28–31] based on their endogenous auto-fluorescence. Combination of OCT and TPL imaging can provide both scattering and absorption/emission contrast from native tissue and simultaneously detect plaque structure and composition with high sensitivity, specificity and spatial resolution. To the best of our knowledge, a combined OCT and TPL imaging approach was first introduced by Beaupaire, *et al* in 1999 [32], similar systems were later demonstrated by Tang *et al* [33] and Vinegoni *et al* [34], respectively, in 2006. All these systems utilized a single light source (i.e., same wavelength) for OCT and TPL microscopy and were based on bulk optics. Jeong *et al* described a bulk-optics-based combined system using individually optimized light sources for OCT and TPL microscopy in 2011 [35]. Wang *et al*, in 2014, demonstrated a bulk-optic probe-based OCT and TPL microscopy system but with OCT/TPL images recorded separately and not co-registered [36]. Further, Xi *et al* reported an integrated OCT and TPL imaging platform using a customized photonic crystal fiber and endoscope in 2012 [37]. Although this system was fully fiber-based, only *en face* OCT and TPL images (with contrast agent) were obtained due to the high numerical aperture (NA = 0.8) beam incident on the sample as well as limited power of the TPL excitation light source (~155 mW).

In this study, we implemented for the first time a dual-modality fiber-based OCT-TPL imaging system using a photonic crystal fiber that can generate co-registered 3D OCT and 2D TPL images. We demonstrated that TPL imaging in combination with OCT can identify plaque composition (e.g., lipid and oxidized-LDL) with high resolution in the context of surface profile of the vessel lumen without using contrast agent. Presence of lipid in plaques was confirmed by histology. This dual-modality imaging approach can reveal molecular composition within a fully co-registered anatomical microstructural image of the coronary artery in 3D and has the potential to be adapted to the clinical environment for intravascular imaging using a photonic crystal fiber-based catheter.

## 2. Materials and methods

### 2.1 Sample preparation

A metallic sample (stainless steel ruler) was used to show the TPL excitation of metal and detection of TPL emission at long wavelengths (i.e., 640-720 nm).

A tissue sample (atherosclerotic human coronary arteries) was used to demonstrate the capability of TPL imaging of lipid at short wavelengths (i.e., <640 nm) in combination with OCT for plaque microstructure delineation. Human hearts from two male donors aged 55 and 62 years were received from the South Texas Blood and Tissue Center and evaluated within 48 hours of death. The Institutional Review Board (IRB) at the University of Texas Health Science Center in San Antonio approved this study. The left anterior descending artery (LAD), left circumflex artery (LCX) and right coronary artery (RCA) were carefully dissected from each heart, cut open, and positioned *en face* with the luminal side facing up for OCT-TPL imaging at a field of view (FOV) of  $1.6 \times 1.6 \text{ mm}^2$ . Atherosclerotic plaques were identified visually by a yellow coloration representing lipid near the luminal surface. A total of twenty FOVs with suspected plaques were imaged and marked with Indian ink for co-registration with histology.

### 2.2 Fiber-based OCT-TPL imaging system

The fiber-based dual-modality OCT-TPL imaging system incorporated swept-source OCT and TPL imaging modules and scanning optics (Fig. 1). The custom-built intensity OCT module used a swept-source laser (HSL-2000, Santec, Hackensack, NJ) with a center

wavelength of 1,310 nm and a bandwidth of 80 nm scanning at a repetition rate of 20 kHz. Average power incident on the sample was 0.5 mW. The measured free-space axial resolution was 20  $\mu\text{m}$  (~15  $\mu\text{m}$  in tissue) with a 5.1 mm scan depth determined by 704 pixels/A-scan and 7.2  $\mu\text{m}$ /A-scan pixel measured in air. The custom-built TPL imaging module utilized a femtosecond Ti:Sapphire laser (Mai Tai HP, Newport, Irvine, CA) with excitation tunable over 760-1040 nm (80 MHz). TPL emission from sample was reflected by a 720 nm long-pass dichroic mirror (Prairie Technologies, Middleton, WI) to block the excitation laser line and collected by two photomultiplier tubes (PMT1: H7422P-40, PMT2: R3896, Hamamatsu, Bridgewater, NJ) in spectral ranges of 640-720 nm and <640 nm, respectively, to distinguish endogenous chromophores in the plaque (e.g., lipid deposits) and exogenous chromophores such as metal. To eliminate the PMT photon count from excitation laser light, a short-pass filter (et720sp, Chroma Technology, Bellows Falls, VT) was placed after the dichroic mirror. A custom-designed adjustable dispersion compensator was utilized to provide transform-limited TPL excitation pulses incident on the sample, comprised of a diffraction grating (1200 lines/mm, Wasatch Photonics, Logan, UT), a focusing lens ( $f = 100$  mm, Thorlabs, Newton, NJ), a polarizing beamsplitter (PBS122m, Thorlabs, Newton, NJ), a half-wave plate (WPH05M808, Thorlabs, Newton, NJ), a quarter-wave plate (WPQ05M808, Thorlabs, Newton, NJ) and a mirror (BB1-E03, Thorlabs, Newton, NJ).

OCT and TPL modules shared a common sample path by using two dichroic mirrors (760DCXRU, T970DCSPXR-XT, Chroma Technology, Bellows Falls, VT). A photonic crystal fiber (PCF, LMA-15, NKT Photonics, Birkerød, Denmark) with a 15  $\mu\text{m}$  diameter core was used to simultaneously transmit single-mode OCT and TPL excitation/emission light to/from the sample. The scanning optics consisted of a doublet PCF collimator ( $f = 40$  mm, Edmund Optics, Barrington, NJ), x- and y-galvanometers (6M2205S-S, Cambridge Technology, Bedford, MA), and a triplet scanning lens ( $f = 50$  mm, Edmund Optics, Barrington, NJ). All lenses were AR-coated. OCT and TPL excitation beam diameters (i.e., lateral resolution) on the sample were both calculated to be ~16  $\mu\text{m}$  based on the similar mode field diameters (i.e., 12.6  $\mu\text{m}$  and 12.8  $\mu\text{m}$ , respectively) of the PCF core at 800 nm and 1,310 nm and magnification of the scanning optics [38]. OCT images were displayed using a logarithmic intensity scale ( $20 \times \log(V_{\text{OCT}})$ ). The OCT-TPL image size was  $512 \times 512$  pixels covering an FOV of  $1.6 \times 1.6$  mm<sup>2</sup>. Because the OCT laser has a repetition rate of 20 kHz compared to 80 MHz of the TPL excitation laser, imaging time was limited by OCT and determined to be 13.1 s (i.e., 25.6 ms/OCT B-can  $\times$  512 B-scans).

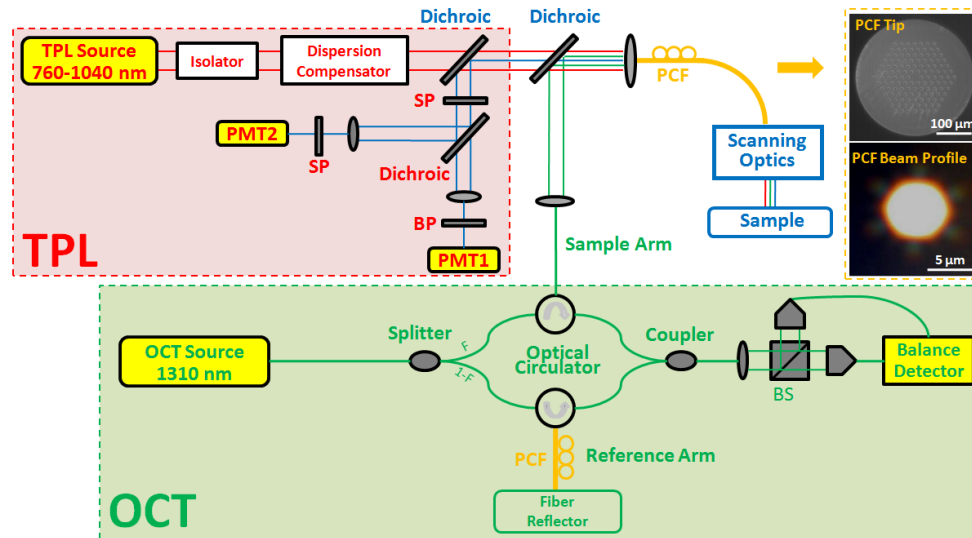


Fig. 1. Schematic diagram of the dual-modality fiber-based OCT-TPL imaging system consisting of OCT and TPL modules and scanning optics. Light from OCT and TPL modules are combined by dichroic mirrors (blue) and a photonic crystal fiber (yellow). Top-view and beam profile of the PCF are shown in the top-right corner. PCF: photonic crystal fiber; PMT: photomultiplier tube; BP: band pass; SP: short pass; BS: beamsplitter.

### 2.3 Histology analysis

After imaging, human coronary arteries were immersion-fixed in 10% neutral buffered formalin, frozen in optical cutting temperature medium, cut into sections 4  $\mu\text{m}$  thick and stained with Oil Red O (ORO) for lipid [39] and Verhoeff-Masson Tri-Elastic (Tri-Elastic) for collagen/elastin fibers [40].

## 3. Results

### 3.1 Custom-designed pulse compensator for TPL excitation

We measured the pulse duration at the output of the TPL excitation laser (800 nm) to be 118.8 fs (Fig. 2(c)). The pulse duration on the sample was significantly stretched ( $>500$  fs) due to group delay dispersion (GDD) after propagating through a 1 m long PCF and optics in the sample path of TPL excitation. A pulse compensator was utilized to restore the pulse duration to a near transform-limited value and maintain sufficient instantaneous power for TPL excitation of chromophores in the sample. We designed and constructed a dedicated pulse compensation system based on a single transmission diffraction grating first suggested by Martinez [41,42], shown in Fig. 2(a). For this configuration, the GDD introduced to the pulse is defined in the following equation [41]:

$$GDD = \frac{\lambda^3}{\pi c^2 s^2 \cos^2 \theta_0} (f - z)$$

where  $\lambda$  (nm) is the center wavelength of TPL excitation light,  $c$  (m/s) is the speed of light,  $s$  (mm/line) is the groove spacing of the grating,  $\theta_0$  is the emergence angle of the beam off the grating,  $f$  (mm) is the focal length of the lens, and  $z$  (mm) is the separation between the grating and the lens, which can be varied to compensate different levels of GDD. With a TPL excitation laser wavelength of 800 nm, a grating groove spacing of 1200 lines/mm, a lens focal length of 100 mm, and an emergence angle of  $\sim 28^\circ$ , GDD imparted to the laser pulse is  $3,345 \text{ fs}^2/\text{mm} \times (f - z)$ . Thus for the predicted PCF GDD of  $45,200 \text{ fs}^2/\text{m}$  (LMA-15), 1 meter

of PCF can be accommodated by setting  $z$  to approximately 114 mm. Zemax simulation of GDD (computed from optical path length versus wavelength) for the pulse compensator (Fig. 2(b)) is in agreement with that calculated by the equation above. For minimum pulse duration on the sample, the actual distance of  $z$  was set to 117 mm to compensate GDD originating in the optics in the sample path of TPL excitation (e.g., isolator, lenses, beamsplitter, and dichroic mirrors). Pulse duration incident on the sample was restored and measured to be 122 fs, very close to that at the output of the TPL excitation laser (118.8 fs).

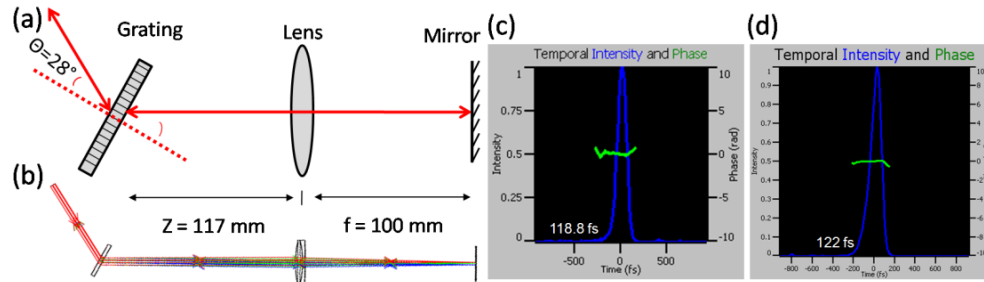


Fig. 2. (a) Schematic diagram of the custom-designed pulse compensator comprised of a transmission diffraction grating, a focusing lens and a mirror. (b) Zemax simulation of optical path length and GDD with ray tracing for the pulse compensator configured in (a). Ray colors in (b) represent spectral bandwidth of the TPL excitation laser centered at 800 nm (i.e., 795–805 nm). (c,d) Temporal intensity and phase measurement of pulse duration at the output of TPL excitation laser (800 nm) and on the sample after employing the pulse compensator, respectively. Pulse intensity and phase were characterized using an ultrashort-laser-pulse measurement device (Grenouille, SwampOptics, Atlanta, GA).

### 3.2 OCT-TPL imaging of metallic sample

Metals are known to exhibit strong TPL emission when excited with ultrashort pulsed radiation [43]. TPL emission from metals is characterized by a broad emission wavelength range (e.g., 350–800 nm) with spectral intensities increasing at longer wavelengths where the TPL excitation is located (e.g., 800 nm). Metal nanoparticles, especially gold nanoparticles, with different coatings have been developed to target various cellular/molecular components in tissues for diagnostic and/or therapeutic applications due to their unique optical properties, negligible cytotoxicity and good biocompatibility [44–51]. Gold nanoparticles demonstrate strong absorption contrast under TPL excitation, and therefore, can be utilized to target plaque composition that does not have strong endogenous TPL emission (e.g., macrophages). Here we performed OCT-TPL imaging on a metallic sample to demonstrate TPL imaging to detect the metallic composition of the sample. Figure 3 shows dual-modality OCT-TPL imaging of a stainless steel ruler. The numeral “8” and scale bars are visualized in the *en face* OCT (Fig. 3(a), 3(d)), TPL (Fig. 3(b), 3(e)) and merged OCT-TPL (Fig. 3(c), 3(f), 3(g)) images. TPL images show a strong emission signal from stainless steel at an incident excitation power or energy density of  $1.96 \times 10^{-4} \text{ W}/\mu\text{m}^2$  or  $7.84 \times 10^{-10} \text{ J}/\mu\text{m}^2$ . More detailed features of the target are evident (e.g., isolated bright spots in Fig. 3(b), 3(e)), caused by inhomogeneities or surface roughness of the material [52,53]. When a 2D *en face* OCT image or a 3D OCT image is merged with the co-registered TPL image, surface structure and composition of the target (i.e., stainless steel ruler) are depicted simultaneously. Of note is that most TPL emission from stainless steel is constrained within a longer wavelength range (640–720 nm) and detected by PMT1, whereas much lower TPL emission is captured by PMT2 (data not shown), consistent with spectral characteristics of metallic TPL emission [43,52,54].

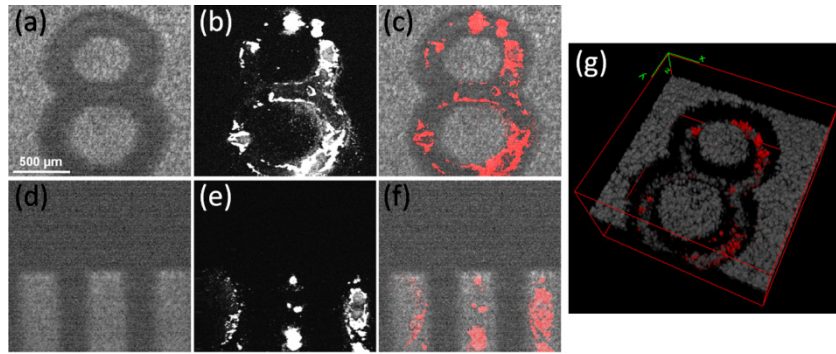


Fig. 3. Dual-modality OCT-TPL imaging of a stainless steel ruler. *En face* OCT (a,d), co-registered TPL (b,e), and merged OCT-TPL (c,f) images of numeral “8” and scale bars, respectively, on the ruler. (g) 3D OCT image set merged with the TPL image, showing composition of the ruler in the context of its surface structure. Red indicates TPL emission in (c,f,g).

### 3.3 OCT-TPL imaging of tissue sample

Dual-modality OCT-TPL imaging of human coronary arteries was used to demonstrate simultaneous detection of plaque structure and composition. To detect TPL emission from native tissue, a higher TPL excitation power or energy density compared to the metallic sample was applied ( $\sim 1.96 \times 10^{-3} \text{ W}/\mu\text{m}^2$  or  $7.84 \times 10^{-9} \text{ J}/\mu\text{m}^2$ ). As the spectral ranges of TPL emission from native plaque components such as oxidized-LDL, lipid, collagen/elastin fibers (in response to an 800 nm TPL excitation) are all much shorter than 650 nm [28,55,56], PMT2 (<640 nm) was utilized to collect most of TPL emission from tissue. OCT and TPL images were recorded and merged into a single image. Figure 4(a) illustrates a TPL image of a plaque region where isolated spots and regions with bright TPL emission are observed. Size of chromophores varies from 5  $\mu\text{m}$  to over 200  $\mu\text{m}$ , suspected to originate from oxidized-LDL particles (small isolated bright spots) and lipid droplets/deposits (large oval-shaped regions) [28]. Brightness of TPL emission is determined by the depth and absorption properties (i.e., two-photon absorption cross-section) of the chromophores as TPL imaging integrates emission signal over a depth of focus of  $\sim 500 \mu\text{m}$  determined from the size of beam waist. Figure 4(b) shows a co-registered *en face* OCT image providing the surface structure of the plaque region. Figure 4(c) is the merged OCT-TPL image that overlays molecular components onto the structural context of the tissue, suggesting good complementarity of OCT and TPL imaging. A 3D OCT data set is then merged with the TPL image (Fig. 4(d)), demonstrating chromophore distributions in relation to the tissue surface profile. Figure 4(e) shows a B-scan OCT image at the white dashed line in Fig. 4(a). Lower back scattered OCT signal (yellow dashed boxes in Fig. 4(e)) corresponds to plaque components with less scattering (e.g., lipid deposits), which is inversely represented by higher intensity regions (red curve in Fig. 4(e)) of TPL emission signal profile along the white dashed line in Fig. 4(a). This further demonstrates the complementary characteristics of OCT and TPL imaging in atherosclerotic plaque detection.

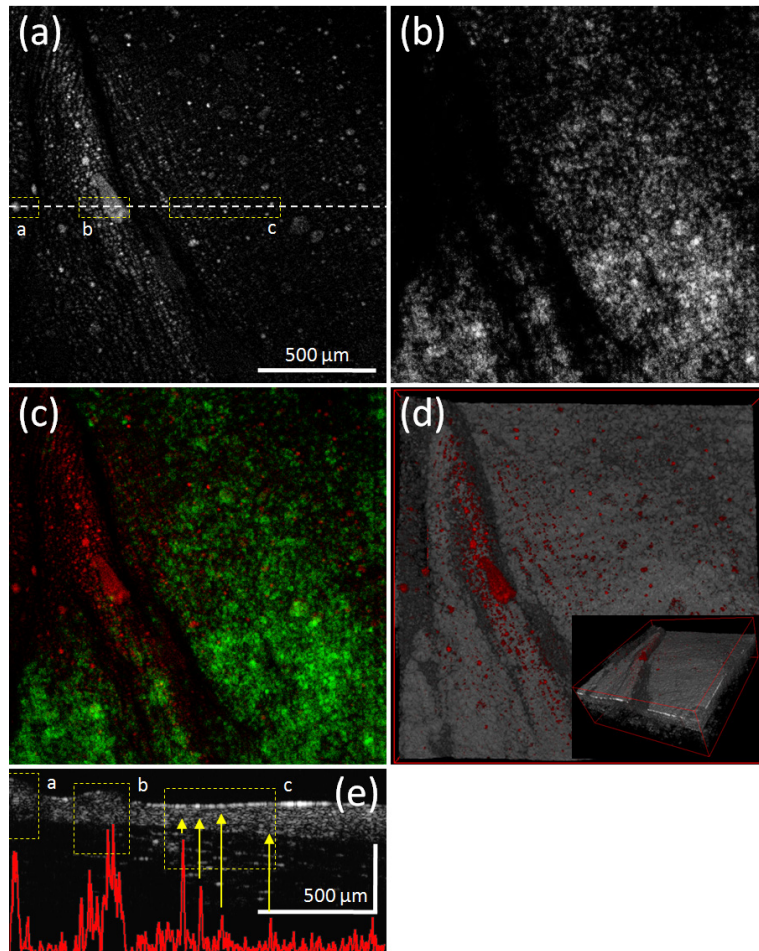


Fig. 4. Dual-modality OCT-TPL imaging of a human coronary artery. TPL (a), *en face* OCT (b), merged *en face* OCT-TPL (c), merged 3D OCT-TPL (d) images of the plaque region. Red in (c,d) indicates TPL signal measured at emission wavelengths shorter than 640 nm while green in (c) represents back scattered OCT signal. The inset image in (d) shows the merged 3D OCT-TPL image at a different angle. (e) B-scan OCT image at the white dashed line in (a). Higher intensity regions of the TPL emission signal profile (red curve in (e), a.u.) at the white dashed line in (a) correspond to lower intensity regions (yellow dashed boxes “a,b,c”) in the B-scan OCT image. Yellow arrows point to small regions of lower scattering intensity in dashed box “c”.

To investigate origin of the TPL emission signal, 4  $\mu\text{m}$  thick tissue sections were cut after imaging for histology with ORO stain for lipid and Tri-Elastic stain for collagen/elastin fibers. Figure 5 shows another example of OCT-TPL imaging of a plaque region. In the TPL image, isolated spots with bright TPL emission (yellow dashed box “b” in Fig. 5(a)) are visualized. Moreover, curved structures, such as the curves in the yellow dashed box “a” in Fig. 5(a), are also observed. In contrast, the co-registered *en face* OCT image (Fig. 5(b)) shows lower signal in the regions with higher TPL emission. The merged *en face* OCT-TPL image (Fig. 5(c)) demonstrates how TPL bright spots and curved structures of higher TPL intensity (red) complement the lower intensity regions of OCT (green). Adjacent tissue sections at the white dashed line were stained with ORO (Fig. 5(e)) and Tri-Elastic (Fig. 5(f)), respectively. Red regions in the ORO section (yellow dashed boxes in Fig. 5(e)) correlate well with the higher TPL intensity regions in the yellow dashed boxes along the white dashed line in Fig. 5(a), indicating that the isolated bright spots and curved structures may originate

from oxidized-LDL particles and/or lipid droplets/deposits in the plaque. Collagen fibers (green in Fig. 5(f)) shown in the Tri-Elastic section are across the entire tissue surface, but the TPL signal is only apparent in regions of lipid, suggesting that collagen/elastin fibers may not contribute to the TPL emission signal at the excitation power density used in this region of interest. The B-scan OCT image (Fig. 5(g)) at the white dashed line in Fig. 5(a) provides a consistent co-registration of lipid regions between TPL and the histology image (yellow dashed boxes “a,b” in Fig. 5(a), 5(e), 5(g)). To further demonstrate the location of lipid deposits in the tissue, the TPL image is overlaid onto the context of a 3D OCT data set (Fig. 5(d)) where tissue regions with fatty streaks [57] are evident. Isolated bright spots and curved structures are closely correlated in the TPL image. Bright spots “grow” and are replaced by curved structures from top-right to bottom-left in Fig. 5(a), indicating a possible transition region from isolated lipid droplets and/or oxidized-LDL particles to fatty streaks on the luminal surface of the vessel.

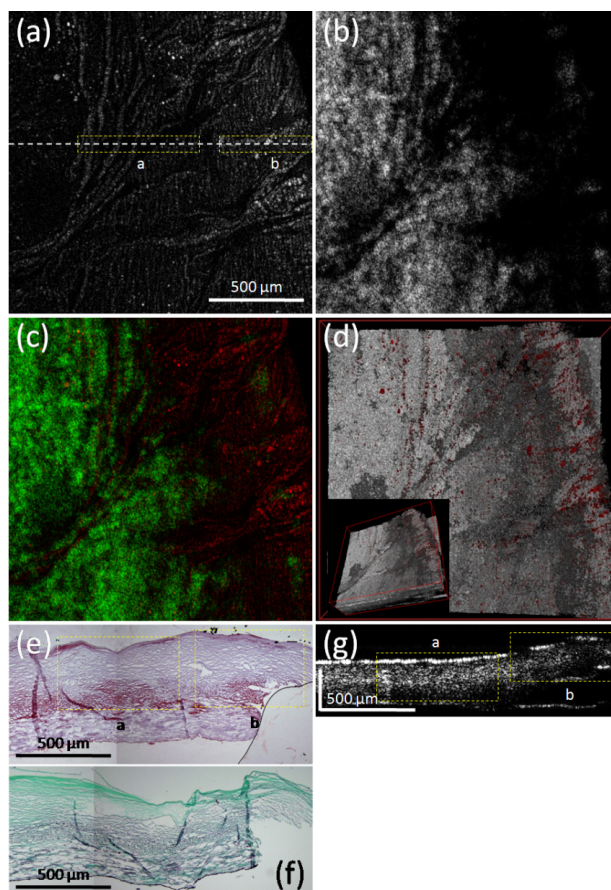


Fig. 5. Dual-modality OCT-TPL imaging of a human coronary artery and corresponding histology. TPL (a), *en face* OCT (b), merged *en face* OCT-TPL (c), merged 3D OCT-TPL (d) images of the plaque region. Red in (c,d) indicates TPL signal measured at emission wavelengths shorter than 640 nm while green in (c) represents back scattered OCT signal. The inset image in (d) shows the merged 3D OCT-TPL image at a different angle. (e,f) ORO and Tri-Elastic stains of a histological tissue section at the white dashed line in (a), showing lipid deposits (red) and collagen (green)/elastin (black) fibers respectively. (g) B-scan OCT image at the white dashed line in (a). Lower intensity regions (yellow dashed boxes “a,b” in (g)) are represented by higher intensity regions (yellow dashed boxes “a,b” in (a)) along the white dashed line in the TPL image and are consistent with histology (yellow dashed boxes “a,b” in (e)).

#### 4. Discussion

IVOCT is a recently developed catheter-based method for high-resolution imaging of coronary arteries. The high axial resolution of IVOCT ( $\sim 10\ \mu\text{m}$ ) has generated considerable interest as a candidate method to assess atherosclerotic plaques [58]. Of all clinically available cardiovascular imaging modalities, IVOCT is the sole approach that provides sufficient spatial resolution to detect and image thin fibrous caps. But unfortunately, when the cardiologist observes a plaque in an IVOCT image, inaccuracies may occur in classifying the plaques and evaluating the risk of plaque rupture only based on tissue structures. Yabushita *et al* characterized plaque types by OCT signal levels and boundaries between fibrous, fibrocalcific, and lipid-rich plaques. Plaque types may be misinterpreted due to OCT penetration depth and if multiple molecular components (i.e., lipid, calcium) exist in the same plaque [59]. Phipps *et al* recently observed that sharp changes in tissue index of refraction (i.e., higher back scattering signal in IVOCT images) may be caused by macrophages, fibrous tissue, interfaces between calcium and fibrous tissue, calcium and lipid, and/or fibrous-cap and lipid pool [60]. As a result, plaque types cannot be accurately classified unless cellular/molecular compositions of the plaque can be detected (not inferred from tissue structure by OCT). Two-photon luminescence (TPL) microscopy has been applied for *ex vivo* or *in vivo* (with blood vessels exposed) plaque component characterization based on endogenous auto-fluorescence emission under TPL excitation [28–31], which has the potential to correct the above inaccuracies by determining the cellular/molecular composition of plaques in the context of structures elucidated by OCT. However, delivery of ultrashort laser pulses to the plaque *in vivo* through a conventional glass fiber represents a technical challenge because of the risk of damage to the fiber caused by high optical powers (e.g.,  $>10\ \text{W}/\mu\text{m}^2$  instantaneous power density). Photonic crystal fiber (PCF) offers the unique capability to transmit high power ultrashort laser pulses while maintaining single mode beam quality over a wide wavelength range, critical for both TPL imaging and OCT. In this study, the two imaging modalities were combined in a PCF to transmit single mode OCT and TPL excitation light, and endogenous TPL emission light from tissue for the first time, providing identical laser spot size (i.e., lateral resolution) on the sample.

TPL microscopy has demonstrated two-photon absorption/emission contrast of intracellular and extracellular lipid droplets/deposits and oxidized-LDL particles, all of which emit and are detected at short wavelengths ( $<640\ \text{nm}$ ) [28–31], consistent with our observation in this study. Our results suggest that TPL imaging provides complementary optical contrast to OCT which is based on light scattering caused by refractive index gradients in tissue, and specifically identifies key plaque component such as lipid that does not exhibit strong light scattering in OCT. Merged OCT-TPL images simultaneously show plaque structure and composition, significantly enhancing the opportunity to identify, evaluate and characterize atherosclerotic plaques based on cellular/molecular composition of the plaques with high resolution, sensitivity and specificity. In addition, due to the specificity of TPL imaging for detection of metal at long wavelengths (640–720 nm), targeted imaging approaches (e.g., gold nanoparticles) could be helpful in identifying macrophages that do not have sufficient endogenous TPL or OCT contrast over other plaque components [61]. Further, TPL imaging could be useful for improved monitoring of drug eluting metallic stents [62] over time.

As the depth of focus of the TPL excitation beam is  $\sim 500\ \mu\text{m}$ , TPL emission from chromophores within this range is detected and integrated. Figure 6(a) shows TPL detection of lipid droplets/deposits and/or oxidized-LDL particles located beneath the surface of the plaque. Isolated bright spots (yellow dashed box “a” in Fig. 6(a)) and large bright regions (yellow dashed box “b” in Fig. 6(a)) at the white dashed line in the TPL image co-register with lower signal regions of the corresponding B-scan OCT image (Fig. 6(c)). ORO stain of lipid demonstrates a big lipid pool located at approximately 250–750  $\mu\text{m}$  in depth (yellow

dashed boxes “a,b” in Fig. 6(b)), suggesting that the bright TPL emission can be generated from lipid deep in the tissue and demonstrating the capability of OCT-TPL imaging to detect chromophores deeper than 200  $\mu\text{m}$  underneath plaque surface. Worth noting is that size of lipid features in the TPL image varies with locations of the lipid pool (yellow dashed boxes “a,b” in Fig. 6(a)), although the histology image (Fig. 6(b)) shows similar ORO stain color and depth at these locations.

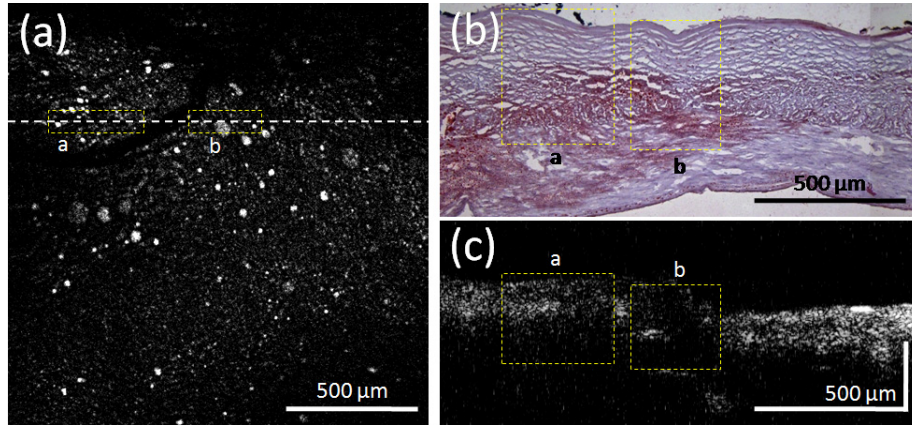


Fig. 6. (a) TPL image of the plaque region. (b) ORO stain of a histological tissue section at the white dashed line in (a), showing a lipid pool (red) deep in the tissue. (c) B-scan OCT image at the white dashed line in (a). Lower intensity regions (yellow dashed boxes “a,b”) in the B-scan OCT image (c) are represented by higher intensity regions along the white dashed line in the TPL image (yellow dashed boxes “a,b” in (a)) and consistent with the lipid locations in the histology image (b).

A novel dual-modality OCT-TPL imaging system is demonstrated in this study for *ex vivo* atherosclerotic plaque characterization using a PCF. Therefore, clinical translation of this dual-modality fiber-based system to a catheter-based imaging system appears feasible. Yoo *et al* developed an intra-arterial catheter for combined optical frequency domain imaging (OFDI) and NIRF imaging using a double-clad fiber and tested it using a rabbit model with implanted NIR-fluorescent fibrin-coated stent [27]. Similarly, Lorensen *et al* proposed a needle probe for combined OCT and fluorescence imaging using an excised sheep lung with fluorescein solution infused through the vasculature [63]. Recently, Xi *et al* implemented an integrated OCT and TPL imaging platform using a customized double-clad PCF and endoscope on contrast-enhanced (with ICG administration) mouse tissues [37]. Due to similar structure and mechanics of the dual-modality catheter to standalone OCT catheters currently used in the cardiac catheterization laboratory [64], future development of the OCT-TPL imaging catheter (i.e., using a PCF) to detect lipid sub-types (i.e., lipid droplets/deposits and oxidized-LDL particles) and possibly other plaque compositions *in vivo* is feasible.

In the currently study, OCT incident power on the sample was 0.5 mW, to achieve higher incident power as well as higher axial resolution ( $\sim 5 \mu\text{m}$  in tissue) and faster imaging speed, a higher power and repetition rate OCT laser source with a broader bandwidth, and a better fiber coupling strategy may be employed. As can be observed from the OCT images in Fig. 4(e), Fig. 5(g) and Fig. 6(c), speckle size is larger compared to those obtained from standard OCT systems. This deficiency is due in part to use of a PCF. Speckle size is impacted by mode field diameter (MFD) of the fiber acting as a pinhole to receive back scattered OCT light. Because the MFD of the PCF (12.8  $\mu\text{m}$ ) is larger than that of a standard single mode fiber (SMF-28, 9.2  $\mu\text{m}$ ), larger speckle size is expected.

Although we identified collagen/elastin fibers in atherosclerotic arteries with histology, these features were not detected in our TPL images in contrast to using TPL microscopy

[28,61]. Detection of collagen/elastin fibers may be possible in a fiber-based system by increasing either the TPL excitation power or collection efficiency of the fiber.

## **5. Conclusion**

In this study, we presented a novel dual-modality fiber-based optical system that combines OCT and TPL imaging using a photonic crystal fiber for the first time. A pulse compensator was employed to restore pulse duration on the sample to be equivalent to the laser output. TPL emission from a metallic (stainless steel ruler) and tissue sample (human coronary arteries) was recorded and distinguished at different emission wavelengths. High intensity TPL signal from lipid-rich plaque regions is in good agreement with lipid distributions in histology, suggesting that the TPL emission is generated by lipid droplets/deposits and/or oxidized-LDL particles both superficially and deep in the tissue. 2D and 3D merged OCT-TPL images show the location and distribution of lipid in the context of plaque structure, demonstrating complementary optical contrast between the two imaging modalities. Our results suggest that dual-modality OCT-TPL imaging is a promising approach for simultaneous microstructural and molecular analysis of atherosclerotic plaques, which substantially improves the diagnostic capability of OCT alone by the addition of two-photon absorption/emission contrast.

## **Acknowledgments**

The authors would like to acknowledge the technical support from Chris Hoy, PhD and Jingjing Sun, ME. This work is supported by ASLMS Research Grant to Wang, Veterans Health Administration Merit Grant (I01 BX000397) to Feldman, American Heart Association Grant (13POST17080074) to Phipps, Research Grant from Clayton Foundation for Biomedical Research to Milner and Feldman, and Biomedical Engineering Advancement Fund from the University of Texas at Austin to Milner.